Large Tunable Perpendicular Magnetic Anisotropy in Ultrathin Co-Based Ferromagnetic Films Induced by Antiferromagnetic δ-Mn

R.K. Han,[1,2] L. Liu,[1,2] H.L. Sun,[1,2] H.R. Qin,[1,2] X.P. Zhao,[3,*] D. Pan,[1,2] D.H. Wei,[1,2] and J.H. Zhao[1,2,†]

[1] *State Key Laboratory of Superlattices and Microstructures, Institute of Semiconductors, Chinese Academy of Sciences, P.O. Box 912, Beijing 100083, China*

[2] *Center of Materials Science and Optoelectronics Engineering, University of Chinese Academy of Sciences, Beijing 100190, China*

[3] *International School of Microelectronics, Dongguan University of Technology, Dongguan 523808, China*

(Received 15 September 2022; revised 22 November 2022; accepted 12 January 2023; published 13 February 2023)

We report on the observation of large and tunable perpendicular magnetic anisotropy (PMA) in Co-based ferromagnetic (FM) films induced by an antiferromagnetic (AFM) δ-Mn layer. The perpendicular anisotropic energy of the bilayers can be manipulated by varying the thickness of the δ-Mn layer and the maximum reaches 2.41×10^7 erg/cm^3. The coercivity of bilayers is also effectively regulated over a broad range from 0.02 to 7.09 T. We demonstrate that this large PMA originates from strong interfacial exchange coupling and the AFM anisotropic energy. In addition, the antisymmetric longitudinal magnetoresistance occurs in the bilayers in the absence of asymmetric geometry or magnetic field. These results enrich our understanding of AFM-induced large PMA in an AFM/FM bilayer system and provide a promising bilayer structure for exploring high-density magnetic memory devices.

DOI: 10.1103/PhysRevApplied.19.024033

I. INTRODUCTION

The Co-based ferromagnetic (FM) films show the advantages of high Curie temperature (Tc) and large saturation magnetization (M_s). In particular, Co-based full-Heusler alloys have attracted much attention because of their high spin polarization [1,2] and low magnetic damping constant (α) [3,4]. Magnetic tunnel junctions (MTJs) with Co-based FM electrodes thus have a large tunnel magnetoresistance ratio at room temperature [5,6]. The rapid development of information technology has led to higher requirements for storage density, power consumption, and the response speed of memory devices. In this regard, materials with perpendicular magnetic anisotropy (PMA) are more desirable than those with in-plane magnetic anisotropy in MTJs [7,8]. Hence, the search for FM films with considerable perpendicular anisotropic energy (K_u) is a crucial topic in spintronics. In general, there are two common types of PMA in Co-based FM thin films. One is magnetocrystalline anisotropy, such as $L1_1$-phase CoPt and tetragonally distorted Mn_2CoAl [9–11]. The other is interface-induced PMA, which can be observed in Co/Pt, Co/Pd, and Pt/Co_2YX/MgO multilayers [12–14]. However, these PMA films usually exhibit disadvantages, such as low K_u, the inability to withstand high-temperature annealing, and difficulty in tuning PMA. Therefore, we try to find alternative PMA materials or sources of PMA.

As is well known, the exchange interaction between antiferromagnetic (AFM) and FM layers may enhance the coercive field ($\mu_0 H_c$) and form an exchange-bias field ($\mu_0 H_{EB}$) in the adjacent FM layer [15]. Generally, $\mu_0 H_{EB}$ and $\mu_0 H_c$ from the interfacial effect are proportional to J_{ex}/t_{FM}, where J_{ex} is the interfacial exchange energy and t_{FM} is the thickness of the FM layer [16,17]. In addition, the AFM layer also has a considerable effect on the magnetic anisotropy of the FM layer [18]. It is found that AFM can induce PMA in an adjacent FM layer due to the interfacial exchange-interaction effect, such as in CoO/Ni, Ni/Mn/Co, Ni/Co/NiMn, and Co/Fe/FeMn systems [19–22]. On the other hand, the transition-metal Mn shows various crystalline-phase structures with a wealth of magnetic properties. The bulk body-centered-cubic (bcc) δ-Mn belongs to the $Im\bar{3}m$ space group with a lattice constant $a = 0.308$ nm and exists above 1406 K [23]. At present, only a few groups have obtained δ-Mn thin films by epitaxial growth on bcc Cr, Fe, and W buffers at room temperature [24–26]. Density-functional-theory calculations suggest that the magnetic structure of δ-Mn is strongly dependent on the lattice constant and

*zhaoxupeng@dgut.edu.cn
†jhzhao@red.semi.ac.cn

the distortion ratios of c/a [23,27]. As the lattice constant increases, the magnetic structure changes from FM to ferrimagnetic and then to AFM. Neutron diffraction shows that δ-Mn on Fe buffer with lattice distortion is AFM [28]. However, the detailed magnetic properties of δ-Mn and its potential applications require further exploration.

Here, we epitaxially grow Al/δ-Mn/Co-based FM multilayers on GaAs (001) substrates and investigate their magnetic and electrical transport properties. It is found that AFM δ-Mn can induce large PMA in various Co-based FM films, including Co, CoFe, Co_3Mn, and the Heusler alloys Co_2MnSi (CMS), Co_2MnGa (CMG), and Co_2FeAl (CFA). The K_u of the bilayers controlled by the thickness of the Mn layer (t_{Mn}) exceeds 2.41×10^7 erg/cm^3. Meanwhile, the $\mu_0 H_c$ of the bilayers can be adjusted over a wide range from 0.02 to 7.09 T. Apart from that, we also observe antisymmetric longitudinal magnetoresistance (MR) caused by a single domain wall in the bilayers. Such Co-based FM/δ-Mn bilayers with controlled PMA may be suitable for perpendicular magnetized magnetic tunnel junctions or domain spintronics.

II. EXPERIMENT DETAILS

The sample stacking structures of Al(3)/Mn(t_{Mn})/Co-based FM(t_{FM})/GaAs buffer(200)/GaAs substrate (thicknesses in nanometers) are fabricated in a twin-chamber molecular beam epitaxy system [Fig. 1(a)]. First, the semi-insulator (SI) GaAs (001) substrate is deoxidized in one chamber and a 200-nm GaAs smoothing layer is grown on it. The substrate is then transferred into another chamber to deposit the metallic multilayers. The Co-based FM films (0.5–1.5 nm) are grown at 150 °C (Co, CoFe, Co_3Mn) and 300 °C (CMS, CMG, CFA), respectively. To suppress the diffusion of Mn atoms, the Mn layer with different thicknesses is deposited after cooling the substrate to room temperature. Finally, a 3-nm-thick Al layer is grown on Mn to prevent surface oxidation. The background vacuum pressure is better than 1×10^{-7} Pa throughout the metal-film growth process. The thickness of metal films is obtained by using a quartz-crystal thickness monitor. X-ray diffraction (XRD) and high-resolution transmission electron microscopy (HRTEM) are used to determine the phase structure and epitaxial relationship of the multilayers. The hysteresis loops and variations of magnetization (M) with temperature of the bilayers are measured by using a superconducting quantum interference device (SQUID). All the samples are fabricated as Hall bar devices by using photolithography combined with Ar-ion-beam etching. Then the electrical transport properties are measured by using a physical property measurement system (PPMS) and a probe station. Moreover, magneto-optic Kerr effect (MOKE) microscopy is used to observe the magnetic domain images.

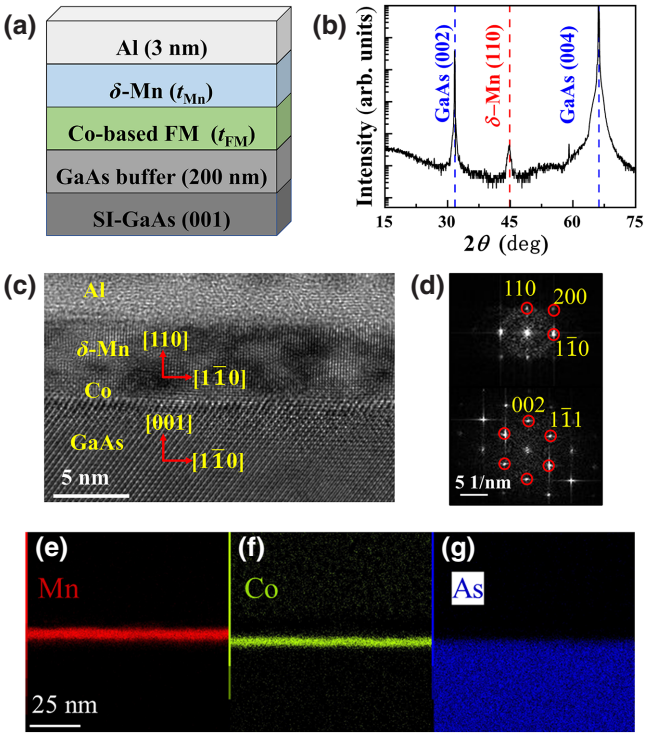

FIG. 1. (a) Stack structure of Al(3)/Mn(t_{Mn})/Co-based FM(t_{FM})/GaAs buffer(200)/GaAs substrate (thickness in nm) multilayers. (b) Corresponding XRD θ-2θ scan pattern at 300 K. Diffraction peak position at 44.65° corresponds to δ-Mn (110). (c) HRTEM image of the multilayers. (d) FFT results for the HRTEM image on the [110] ribbon axis, where the bottom and top panels show the results for GaAs and δ-Mn layers, respectively. Element distribution maps of Mn (e), Co (f), and As (g) atoms in the multilayers.

III. RESULTS AND DISCUSSION

A. Crystal structure of the Co/Mn bilayers

The Co-based FM films (Co, CoFe, Co_3Mn, CMS, CMG, and CFA) are epitaxially grown on GaAs substrates. In particular, the lattice mismatch between them is less than 2%. From the HRTEM image of the Al/Mn/Co/GaAs sample [Fig. 1(c)], an about 5-nm-thick Mn layer exhibits distinct crystal-orientation differences with the GaAs substrate. Figure 1(b) shows the XRD θ-2θ scan pattern for Al(3)/Mn(5)/Co(1.5)/GaAs (thickness in nm) multilayers. The peak position is 44.65°, corresponding to a lattice spacing of $d = 0.202$ nm, which may be the δ-Mn (110) peak or the γ-Mn (111) peak. Combined with the fast Fourier transformation (FFT) results on the [110] ribbon axis [Fig. 1(d)], Mn grown on Co is confirmed to have the bcc structure (δ-Mn) with lattice constants $a = c = 0.286$ nm. The lattice constant of δ-Mn decreases from 0.308 nm at 1406 K to 0.286 nm at 300 K. Furthermore, the epitaxial relationship throughout the multilayers can be derived from the FFT results to be

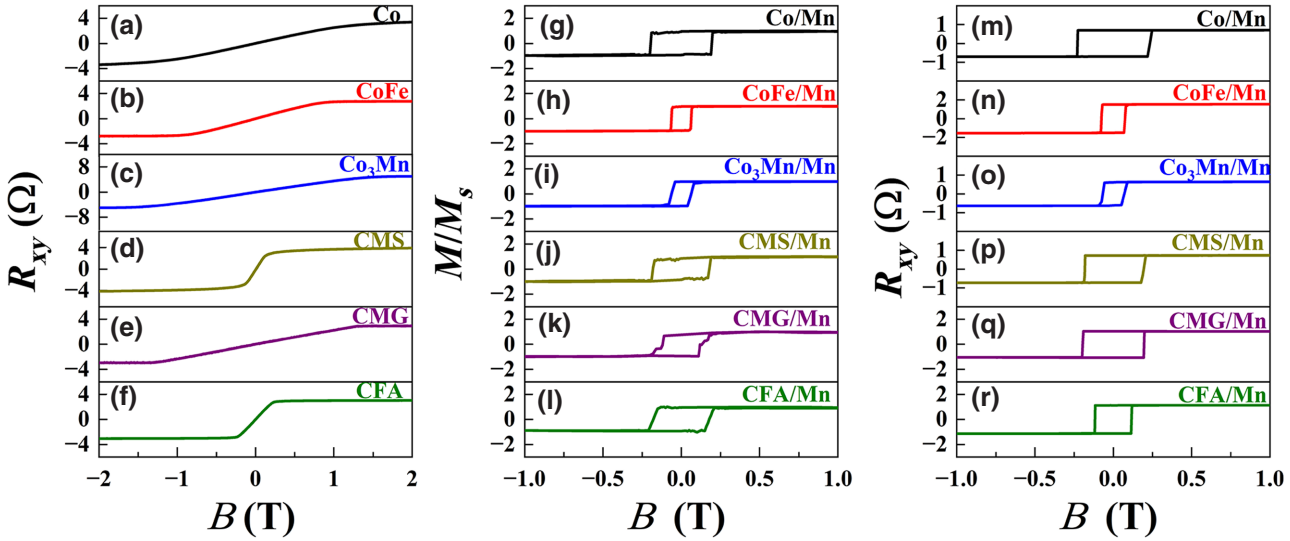

FIG. 2. (a)–(f) Anomalous Hall effect curves of Co, CoFe, Co_3Mn, CMS, CMG, and CFA single layers with a thickness of 1.5 nm at 300 K. (g)–(l) Hysteresis loops of Co-based FM(1.5)/Mn(2) bilayers at 300 K. External magnetic field of ±1 T is scanned along the normal direction of the bilayers. (m)–(r) Anomalous Hall effect curves of the same bilayer samples at 300 K.

Mn(110)[1$\bar{1}$0]||Co(001)[1$\bar{1}$0]||GaAs(001)[1$\bar{1}$0]. This epitaxial relationship differs from the results for δ-Mn grown on Cr, Fe, and W buffers [24–26], and no lattice distortion is observed. There is some diffusion at the interface between Co and GaAs, but there is no obvious diffusion between Co and Mn, thus avoiding alloying, which can be confirmed by the energy-dispersive spectrometer [Figs. 1(e)–1(g)].

B. Perpendicular magnetic anisotropy of the bilayers

The anomalous Hall effect (AHE) curves of the Co-based FM(1.5) single layers are measured by PPMS, and the results [Figs. 2(a)–2(f)] show that the FM single layers all have in-plane anisotropy. Then, we measure the out-of-plane hysteresis loop of the Co-based FM(1.5)/δ-Mn(2) bilayers by using a SQUID. The external magnetic field (B) scans along the normal of thin films within ±1 T. The out-of-plane M-B curves at 300 K are illustrated in Figs. 2(g)–2(l), and the square hysteresis loops reveal that all the bilayers exhibit PMA. Moreover, the AHE curves of the bilayers are also consistent with the M-B results [Figs. 2(m)–2(r)]. Therefore, we can determine that the PMA of the bilayers originates from the interaction between AFM δ-Mn and FM layers. The perpendicular anisotropic energy, $K_u = \mu_0 H_k M_s/2$, responds to the strength of PMA, where $\mu_0 H_k$ and M_s are the perpendicular anisotropy field and saturation magnetization, respectively. In principle, the magnetic moments reach dynamic equilibrium due to the interplay of external magnetic field B and $\mu_0 H_k$. In this case, the total torque (τ_{tot}) exerted on the magnetic moments can be expressed as [29]

$$\vec{\tau}_{tot} = -\gamma \vec{M} \times (\vec{B} + \mu_0 \vec{H}_K) = 0. \quad (1)$$

Hence, the equilibrium formula can be deduced to be

$$\mu_0 H_K \cos\theta_M \sin\theta_M = B(\sin\theta_B \cos\theta_M - \cos\theta_B \sin\theta_M), \quad (2)$$

where θ_M and θ_B represent the angle of FM magnetic moments and B around the z axis, respectively. We measure the variations of anomalous Hall resistance, R_{AHE}, as a function of θ_B. B rotates around the film normal during the measurement, while the magnetic moment rotates with B. First, we obtain θ_M from $R_{AHE} = R_A \cos(\theta_M)$, where R_{AHE} is the experimental value and R_A is the maximum of anomalous Hall resistance. Then $\mu_0 H_k$ of the bilayers is obtained by fitting the R_{AHE}-θ_B curves with Eq. (2). All the R_{AHE}-θ_B curves of the FM(1.5)/Mn(2) bilayers are shown in Figs. 3(a)–3(f), and $\mu_0 H_k$ of all FM(1.5)/Mn(2) samples are 6.43 (Co), 1.99 (CoFe), 4.44 (Co_3Mn), 8.55 (CMS), 9.61 (CMG), and 1.21 T (CFA). Among them, the CMG(1.5)/Mn(2) bilayers possess the largest K_u of 2.41×10^7 erg/cm^3. This allows the lateral size, d, of the MTJs to be scaled to 8.3 nm, when taking into account the thermal stability condition, $K_u d^3/k_B T \geq 60$ [29].

To determine T_N of δ-Mn, we measure the M-T curve of the Co(1.5)/Mn(2) bilayers from 300 to 800 K under a 100-Oe out-of-plane magnetic field [Fig. 4(a)]. The M-T curve shows a magnetic phase transition of the bilayers at 578 K, which is well below the Curie temperature (T_C) of Co (1403 K). We also measure the out-of-plane M-B curves of the bilayers at 600 and 700 K. As

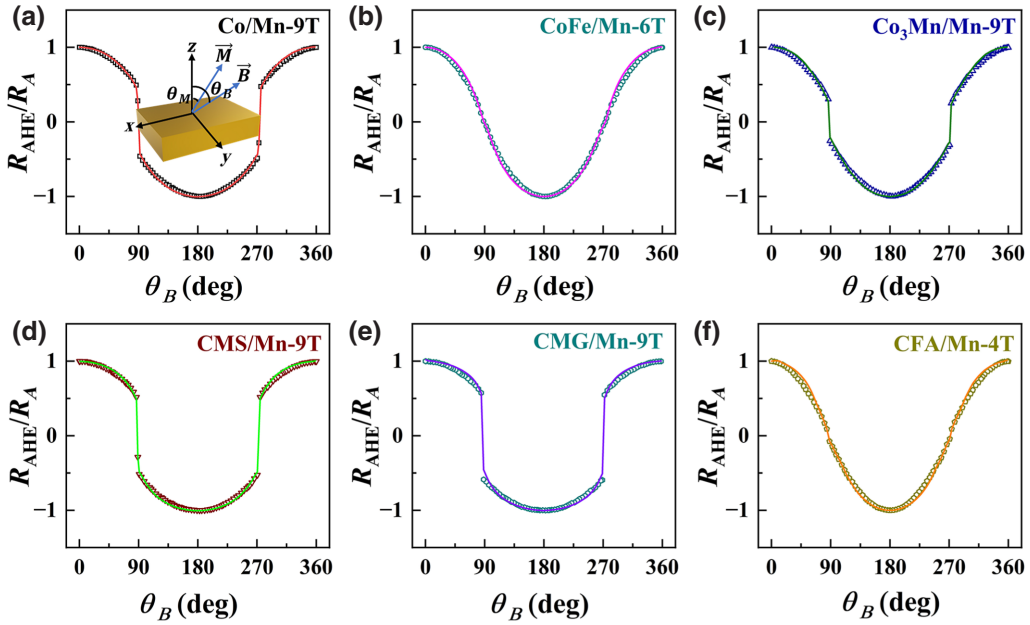

FIG. 3. R_{AHE}/R_A of Co(1.5)/Mn(2) (a), CoFe(1.5)/Mn(2) (b), Co_3Mn(1.5)/Mn(2) (c), CMS(1.5)/Mn(2) (d), CMG(1.5)/Mn(2) (e), CFA(1.5)/Mn(2) (f), bilayers versus θ_B at different external magnetic fields; plots and lines represent experimental results and fitted curves, respectively. Inset in (a) is a schematic diagram of the magnetic moment rotating with B.

shown in Fig. 4(b), the PMA of the bilayers disappears at 600 K, indicating that δ-Mn is not in the AFM state at 600 K. Combining the above results, we infer that the Néel temperature (T_N) of δ-Mn is around 578 K. As is well known, a high thermal-endurance temperature is crucial in the preparation of spintronic devices. We perform high-temperature annealing of the Co(1.5)/Mn(2) bilayers under a B of 0.5 T along the film normal. The AHE curves

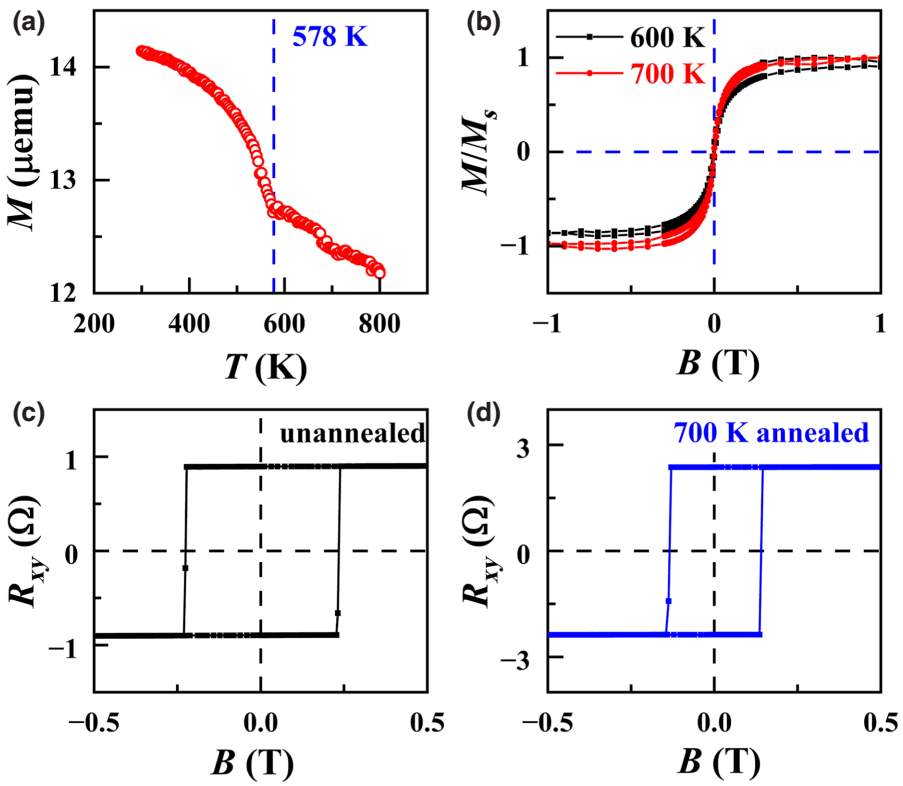

FIG. 4. (a) Out-of-plane M-T curve of the Co(1.5)/Mn(2) bilayers; blue dashed line indicates the phase transition point is 578 K. (b) Hysteresis loops of Co(1.5)/Mn(2) bilayers measured along the out-of-plane directions at 600 K (black) and 700 K (red). Anomalous Hall curves of the Co(1.5)/Mn(2) bilayers, unannealed (c) and annealed at 700 K (d), measured at 300 K.

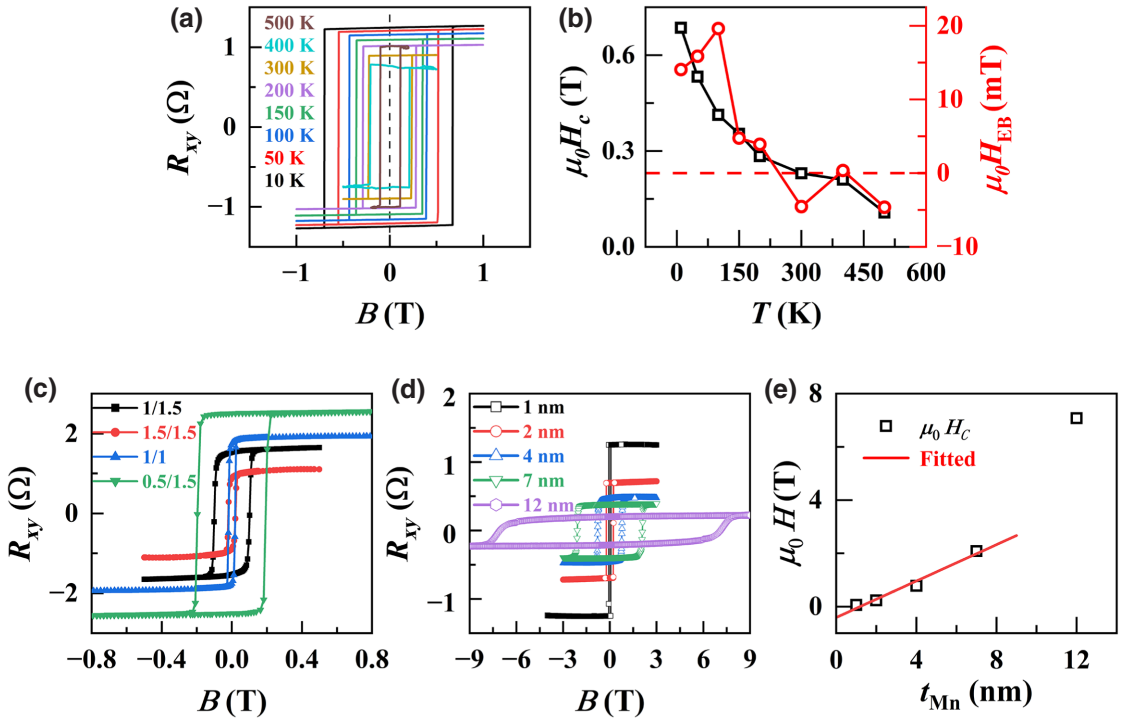

FIG. 5. (a) AHE of the Co(1)/Mn(1.5) sample at different temperatures. (b) Variation of $\mu_0 H_c$ (black) and $\mu_0 H_{EB}$ (red) with temperature from 10 to 500 K. (c) AHE of bilayers with different t_{Co} and t_{Mn}. (d) AHE of Co(1.5)/Mn(t_{Mn}) bilayers, with t_{Mn} from 1 to 12 nm. As t_{Mn} increases, the coercivity increases from 0.02 to 7.09 T. (e) $\mu_0 H_c$ change with t_{Mn}, where the red line is the fitting result.

suggest that the bilayers maintain good PMA after annealing at 700 K [Fig. 4(d)]. The exchange-bias effect is usually observed in FM/AFM bilayers after high-temperature annealing (above T_N) with an applied external field. However, no exchange-bias field is observed in our bilayers, even after 700-K high-temperature annealing with 0.5-T external field.

These Co-based FM films grown on GaAs substrates possess a cubic structure with the [001] crystal orientation. It is well established that their easy axes of magnetization tend to lie in the in-plane direction due to shape anisotropy. Therefore, the observed large PMA in these bilayers can be attributed to the exchange interaction between the FM layer and the AFM layer. Figure 5(a) presents the AHE of the Co(1.5)/Mn(2) sample from 10 to 500 K, where the results above 300 K are measured by the probe station. Obviously, the PMA can be maintained even at 500 K, indicating that the T_N of δ-Mn is higher than 500 K. The coercivity of the bilayers gradually decreases as the temperature increases due to thermal disturbance. The $\mu_0 H_{EB}$ value reaches a maximum of 19.6 mT at 150 K, which is much smaller than the coercivity [Fig. 5(b)]. The AHE of a series of Co(t_{Co})/Mn(t_{Mn}) bilayers with different thicknesses of Co and Mn layers are measured to explore the origin of PMA. Figure 5(c) shows $\mu_0 H_c$ as the function of t_{Co} and t_{Mn}. The $\mu_0 H_c$ gradually decreases with increasing t_{Co} and is roughly the same in Co(1)/Mn(1) and Co(1.5)/Mn(1.5). When t_{Co} is 1.5 nm, the variations of AHE with t_{Mn} from 1 to 12 nm are shown in Fig. 5(d). $\mu_0 H_c$ of the bilayers can reach up to a sizeable value of 7.09 T in the sample of Co(1.5)/Mn(12) bilayers [Fig. 5(e)]. This value exceeds that of most materials with interface-induced PMA. Furthermore, the $\mu_0 H_c$ of bilayers can be effectively tuned between 0.02 and 7.09 T by changing t_{Mn} and t_{FM}. The above results indicate that $\mu_0 H_c$ is not only correlated to t_{FM} but also to t_{AFM}. Figures 6(a)–6(e) shows the R_{AHE}-θ_B curves of Co(1.5)/Mn(t_{Mn}) bilayers with different Mn-layer thicknesses. $\mu_0 H_k$ also increases with t_{Mn} (from 4.1 to 13.0 T), which is obtained by fitting the R_{AHE}-θ_B curves with Eq. (2) [Fig. 6(f)]. When the Mn thickness exceeds 7 nm, $\mu_0 H_k$ is so large that θ_M produces a significant hysteresis, even under an external field of 9 T. To obtain more accurate $\mu_0 H_k$ values, we measure and fit two R_{AHE}-θ_B curves with θ_B from 0° to 360° and 360° to 0°.

C. PMA with different deposition temperatures of Mn layer

The δ-Mn phase exists exclusively at high temperatures, and the only means to obtain δ-Mn at room temperature is by epitaxy on specific buffer layers. To investigate the growth conditions of δ-Mn and the relationship between PMA and δ-Mn in the bilayers, we also deposit Mn

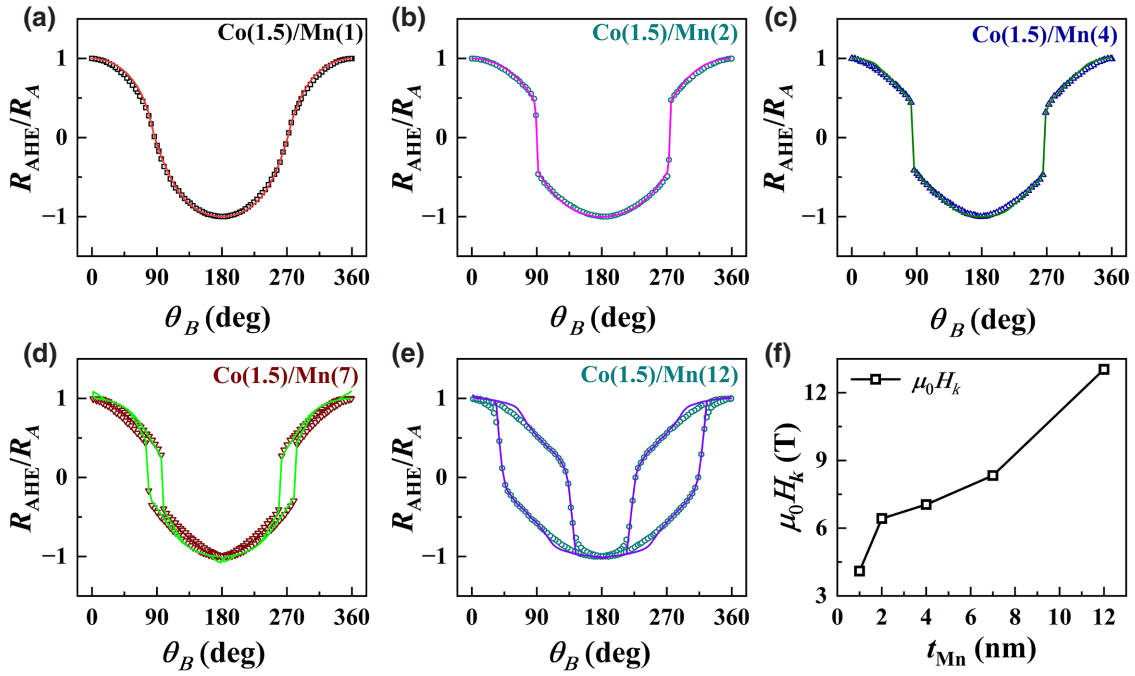

FIG. 6. (a)–(e) R_{AHE}/R_A of Co(1.5)/Mn(t_{Mn}) versus θ_B under the external magnetic field of 9 T; plots and lines represent experimental results and fitted curves, respectively. (f) $\mu_0 H_k$ changes with t_{Mn}.

layers at different temperatures. Figure 7(a) shows the x-ray diffraction patterns of the Al(3)/Mn(4)/Co(1.5)/GaAs (thickness in nm) multilayers with different deposition temperatures of the Mn layer. According to the XRD patterns, only the δ-Mn(110) peak is observed for the Mn layers grown at 40 and 100 °C, and the Mn layers grown at 100 °C have better crystal quality. However, the α-Mn (220) and (330) peaks appear when the deposition temperature of the Mn layer rises above 200 °C. Low-temperature-phase α-Mn is AFM with a complex bcc structure and a T_N of 95 K. In contrast to δ-Mn, α-Mn is the most stable crystal structure at normal temperature and pressure, with 58 atoms in a cubic unit cell. The above results reveal that the phase structure of Mn changes from a pure phase of δ-Mn to a mixed phase of α-Mn and δ-Mn as the growth temperature increases. We measure the AHE of all bilayers to investigate the relationship between the PMA of the bilayers and Mn-layer crystal structure. The AHE curves of Co(1.5)/Mn(4) bilayers with different deposition temperatures of Mn layer indicate the presence of PMA in all bilayers [Figs. 7(b)–7(e)]. The intensity of PMA can be reflected by the rectangularity and, combined with the XRD pattern, the PMA deteriorates when the α-Mn phase appears. Moreover, the Mn layer grown at 100 °C possesses better PMA than that at 40 °C, indicating that PMA depends on the crystal quality of the δ-Mn layer. Therefore, we can determine that the PMA of bilayers depends on the appearance of δ-Mn and its crystalline quality.

D. The origin of PMA

The coercivity of the bilayers decreases with the increase of t_{Co}, implying that the FM/AFM coupling is an interfacial effect. We assume that the PMA of the bilayers originates from interfacial magnetic moment coupling between FM and AFM δ-Mn, and the easy axis of the FM layer changes from in-plane to out-of-plane under the action of J_{ex}. Apart from that, $\mu_0 H_c$ also increases with increasing t_{AFM}. The AFM magnetic moments are usually frozen under B due to the large exchange energy of the sublattices. However, the AFM spins will follow the motion of the FM layer when the antiferromagnetic thickness or anisotropy is sufficiently small to satisfy $K_{AFM} t_{AFM} \ll J_{ex}$, where K_{AFM} is the AFM magnetic anisotropic energy [30–32]. In this case, $\mu_0 H_c$ of the bilayers increases with t_{AFM} until the AFM spins freeze. Moreover, $\mu_0 H_{EB}$ is relatively small because the AFM spin follows the FM spin without pinning of the magnetic moments. This AFM spin motion is directly observed experimentally by x-ray magnetic linear dichroism [33]. In Co-based FM/δ-Mn bilayers, $\mu_0 H_c$ increases, even up to 7.09 T, with increasing thickness of the Mn layer, while $\mu_0 H_{EB}$ is almost zero. It implies that the spin of δ-Mn rotates with the FM layer until t_{Mn} reaches 12 nm. Therefore, $\mu_0 H_c$ and $\mu_0 H_k$ continue to increase with t_{Mn}, while almost no $\mu_0 H_{EB}$ is observed. Ultralarge K_u and $\mu_0 H_c$ not only originate from the strong interfacial exchange coupling between the AFM and FM layers but are also associated with the AFM anisotropic energy.

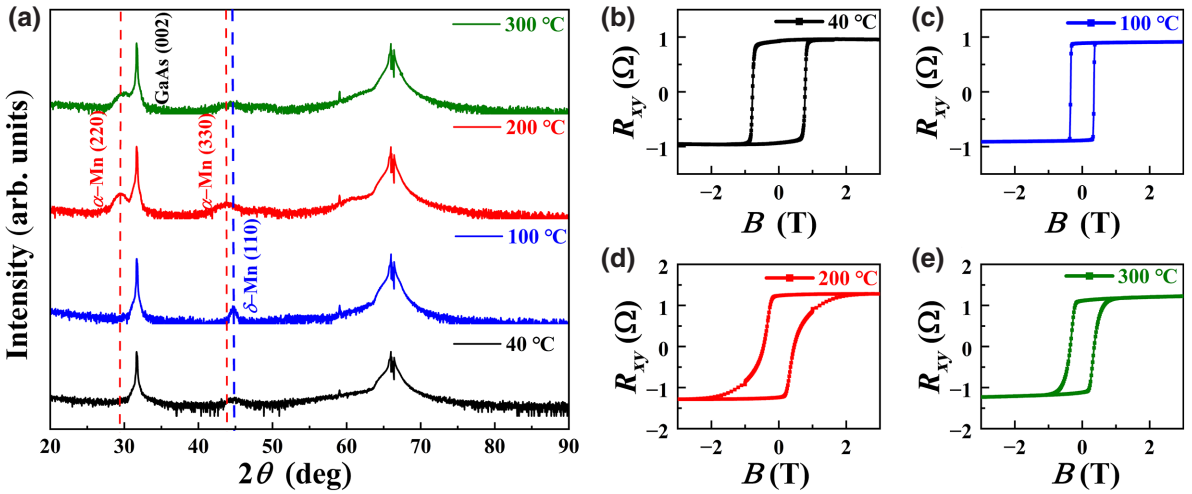

FIG. 7. (a) XRD θ-2θ scan patterns of the Al(3)/Mn(4)/Co(1.5)/GaAs buffer(200)/GaAs substrate multilayers with different Mn-layer deposition temperatures. AHE curves of the Co(1.5)/Mn(4) bilayers with Mn layer deposited at 40 °C (b), 100 °C (c), 200 °C (d), and 300 °C (e).

To further characterize the K_{AFM} of δ-Mn, we consider the uniform-rotation model. For a FM/AFM coupled system, the system energy is

$$E = -HM_{\mathrm{FM}}t_{\mathrm{FM}}\cos(\theta-\beta) + K_{\mathrm{FM}}t_{\mathrm{FM}}\sin^2\beta + K_{\mathrm{AFM}}t_{\mathrm{AFM}}\sin^2\alpha - J_{\mathrm{ex}}\cos(\beta-\alpha), \tag{3}$$

where H is the external magnetic field, M_{FM} is the magnetization of the FM layer, t is the film thickness, and K is the anisotropic energy constant. θ is the angle between H and the z axis, and α and β are the angles between the AFM Néel vector and the FM magnetic moment and the z axis, respectively. The first term is the interaction energy between FM and external magnetic field H, the second term is the FM anisotropic energy, the third term is the AFM anisotropic energy, and the fourth term is the exchange coupling between the FM and AFM interaction energies [31]. By calculating the energy minimum with respect to α and β, we can obtain the coercivity of the bilayers (see Appendix):

$$H_c = \frac{2K_{\mathrm{AFM}}t_{\mathrm{AFM}}J_{\mathrm{ex}}}{2K_{\mathrm{AFM}}t_{\mathrm{AFM}}M_s t_{\mathrm{FM}} + J_{\mathrm{ex}}M_s t_{\mathrm{FM}}}. \tag{4}$$

If $K_{\mathrm{AFM}}t_{\mathrm{AFM}} \gg J_{\mathrm{ex}}$, then $H_c \approx J_{\mathrm{ex}}/M_s t_{\mathrm{FM}}$. H_c is only related to the saturation magnetization, M_s, and thickness of FM. Conversely, if $K_{\mathrm{AFM}}t_{\mathrm{AFM}} \ll J_{\mathrm{ex}}$, then $H_c \approx 2K_{\mathrm{AFM}}t_{\mathrm{AFM}}/M_s t_{\mathrm{FM}}$. H_c is not only related to the thickness of the FM layer, but also to the thickness and anisotropy of AFM. This is consistent with our experimental results. We fit the H_c-t_{AFM} curves [Fig. 5(e)] for Mn-layer thickness ranging from 1 to 7 nm with $H_c = 2K_{\mathrm{AFM}}t_{\mathrm{AFM}}/M_s t_{\mathrm{FM}}$, and the AFM anisotropic energy, K_{AFM}, reaches 1.026×10^6 erg/cm^3. This value is 1 order of magnitude larger than the magnetic anisotropy constant of bcc Co films (-6.5×10^4 erg/cm^3) [34].

E. Antisymmetric magnetoresistance

For conventional PMA materials, the transverse MR (R_{xy}) is antisymmetric with B, while the longitudinal MR (R_{xx}) turns out to be symmetric about external field B. We measure the MR by using a four-terminal sensing method for Hall bars. As shown in Fig. 8(b), the transverse resistance, R_{xy} (R_{AHE}), is obtained by testing at terminals 1 and 3 or 2 and 4, while the longitudinal resistance, R_{xx}, is obtained by testing at terminals 1 and 2 or 3 and 4. Here, we observe the antisymmetric longitudinal MR signal in the Co(1.5)/Mn(1) bilayers, where $R_{xx}(B) = -R_{xx}(-B)$ [Fig. 8(a)]. Combined with the AHE curve, it is found that R_{xx} produces two peaks during magnetization reversal, and the peaks are oddly symmetric about B. We also find that the peak variation of MR with terminals 1 and 2 (R_{12}) is exactly opposite to that with the terminals 3 and 4 (R_{34}), as shown in Fig. 8(c). In addition to this, we measure the MR of Hall bars with two-terminal sensing and the MR of films with four-terminal sensing. The antisymmetric MR peaks are still present in the films but disappear in the Hall bars with two-terminal sensing measurements [Fig. 8(d)]. To investigate the prevalence of this antisymmetric MR, we measure R_{xx} in bilayers of other FM materials as well. The same antisymmetric MR is observed in other FM(1.5)/Mn(2) bilayers [Figs. 9(a)–9(e)]. Furthermore, the antisymmetric MR is also observed in bilayers with different Mn layer thicknesses [Fig. 9(f)]. Compared with the AHE curves, it is found that all the antisymmetric MR signals occur during magnetization reversal.

This antisymmetric MR originates from the potential difference caused by the AHE between the domains with

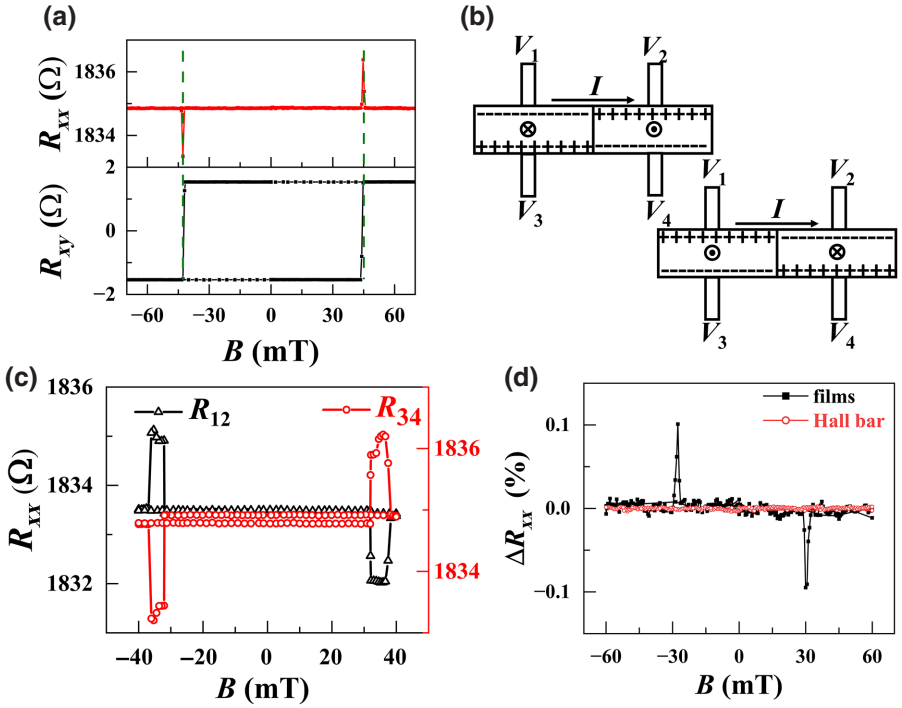

FIG. 8. (a) Longitudinal MR and anomalous Hall effect curves of Co(1.5)/Mn(1) bilayers. (b) Schematic of MR measurement; × (•) indicates that the direction of magnetization is perpendicular to the paper facing inward (outward). (c) Longitudinal MR curves measured through different terminals. (d) Longitudinal MR curves for films (four-terminal sensing) and Hall bar (two-terminal sensing). Vertical coordinate is $\Delta R_{xx} = [R(B) - R(0)]/R(0)$, where $R(B)$ is MR under external magnetic field B.

different magnetization directions, and thus, possessing the same symmetry as R_{xy} [35,36]. As illustrated in Fig. 8(b), we assume that there are only two domains with opposite magnetization directions during the magnetization reversal process of the bilayers, and the domain wall is perpendicular to the current direction. When a current, I, is applied

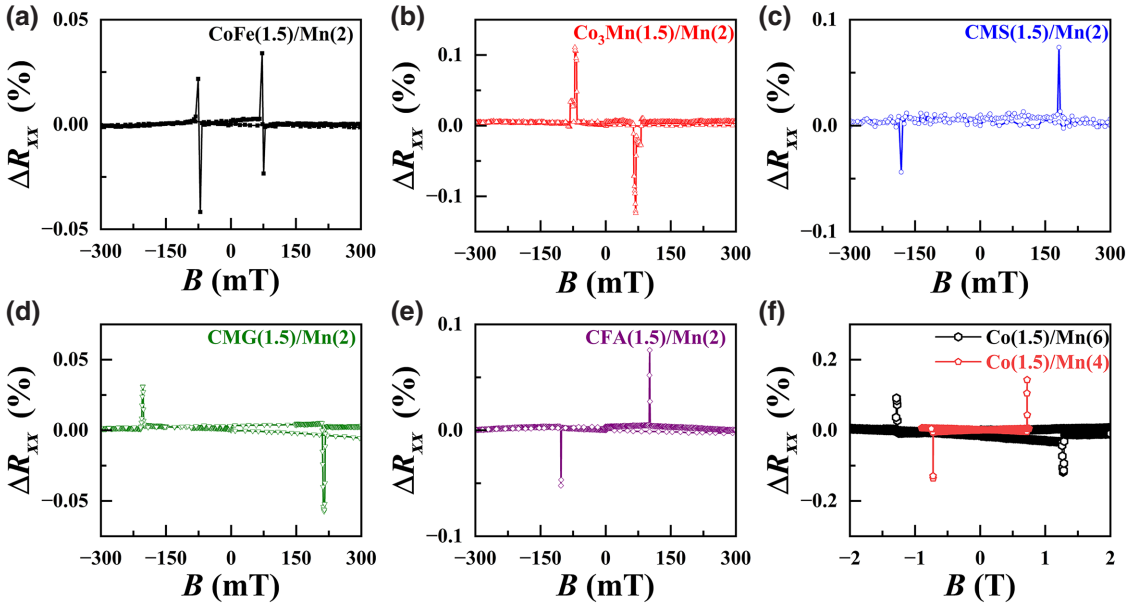

FIG. 9. Antisymmetric MR curves of CoFe/Mn (a), Co_3Mn/Mn (b), CMS/Mn (c), CMG/Mn (d), CFA/Mn (e), and Co(1.5)/Mn(t_{Mn}) (f) bilayers.

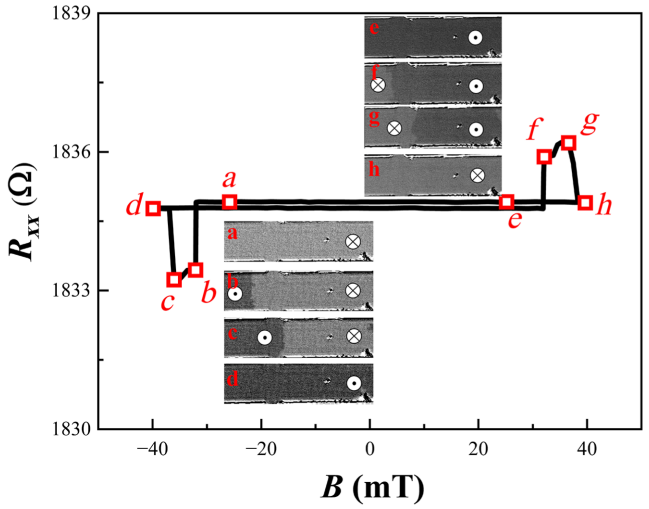

FIG. 10. Magnetic domain images during negative (a)–(d) and positive (e)–(h) magnetization reversal in bilayers. • (×) indicates that the direction of magnetization is parallel to $+z(-z)$.

to the Hall bar, voltages of opposite polarity are generated at the edges of the two domains due to the AHE. When the measurement electrodes are on two separate domains, the motion of the domain wall through the electrode produces an antisymmetric MR peak as B changes. Therefore, the antisymmetric MR peak is actually a manifestation of the AHE signal during the measurement of longitudinal MR. It is obvious that R_{12} and R_{34} have exactly opposite signals, and two-terminal sensing does not show antisymmetric peaks. To verify our conjecture, we observe the magnetic domain images of the Hall bar device using MOKE microscopy. As shown in Figs. 10(a)–10(d), the magnetic moment reversal from $+z$ to $-z$ in the bilayers is dominated by the movement of a single domain wall. In this case, the MR signal caused by the AHE can be obtained by testing the longitudinal MR on the domains in the opposite magnetization direction. At opposite magnetization reversals [Figs. 10(e)–10(h)], the evolution of the magnetic domain structure exhibits similar behavior, and the MR signals are opposite. Therefore, an antisymmetric MR signal is finally obtained, which is consistent with our hypothesis.

For this anomalous MR effect, the appearance of a single domain wall is necessary. The potential differences cancel each other out in multidomains, resulting in the inability to observe the antisymmetric MR signal. However, to reduce the magnetostatic energy, magnetic materials tend to degenerate into multidomains with different magnetization directions. Therefore, the antisymmetric MR is generally not directly observable. Typically, the composition gradients, gradient magnetic fields, and asymmetric Hall bar devices are used to induce the emergence of a single domain wall [37–39]. In our work, there is no asymmetric magnetic field or geometric structure in these bilayers, but the antisymmetric MR is still observed. The AFM is not affected by the magnetostatic energy because the magnetic moments between the AFM sublattices cancel each other out. Thus, it is possible to form larger magnetic domain structures in AFM films. We believe that this may be the reason for the emergence of antisymmetric MR.

IV. CONCLUSION

Co-based FM/Mn bilayers are epitaxially grown on GaAs (001) substrates, in which the Mn layer is bcc structured under the AFM state. A large tunable PMA is obtained in the FM layer induced by the adjacent AFM δ-Mn layer. The PMA of bilayers originates from magnetic moment coupling between the FM/AFM interface and the anisotropy of AFM δ-Mn. The maximum K_u of the bilayers can be controlled by changing both t_{Mn} and t_{FM}, and the maximum reaches 2.41×10^7 erg/cm^3. Interestingly, the coercivity of the FM layer is also adjustable over a wide range, from 0.02 to 7.09 T by altering t_{Mn}. We also observe the antisymmetric longitudinal MR induced by single-domain-wall motion in the bilayers. Therefore, the AFM-induced giant interfacial PMA provides insights into complex exchange interactions in AFM/FM bilayers and supports thermally stable sub-10-nm bits for magnetic memories.

Data that support the findings of this study are available from the corresponding author upon reasonable request.

ACKNOWLEDGMENTS

The work is supported by the Strategic Priority Research Program of the Chinese Academy of Sciences under Grant No. XDB44000000 and the National Natural Science Foundation of China under Grants No. 11834013, No. 12004374, and No. 11874349.

The authors declare that they have no known competing financial interests or personal relationships that could have appeared to influence the work reported in this paper.

APPENDIX: THE COERCIVITY OF FM/AFM BILAYERS

For a FM/AFM coupled system, the system energy is:

$$E = -HM_{\mathrm{FM}}t_{\mathrm{FM}}\cos(\theta-\beta) + K_{\mathrm{FM}}t_{\mathrm{FM}}\sin^2\beta + K_{\mathrm{AFM}}t_{\mathrm{AFM}}\sin^2\alpha - J_{\mathrm{ex}}\cos(\beta-\alpha), \tag{A1}$$

where H is the external magnetic field, M_{FM} is the magnetization of FM layer, t is the film thickness, and K is the anisotropic energy constant. θ is the angle between H and the z axis, and α and β are the angles between the AFM Néel vector and the FM magnetic moment and the

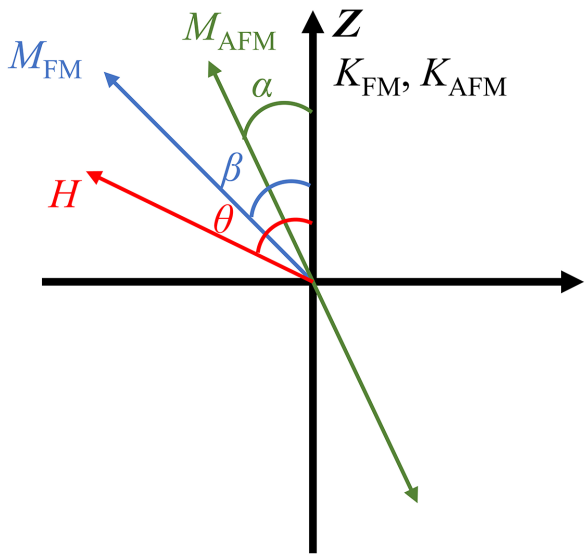

FIG. 11. Schematic diagram of the angles involved in the FM/AFM bilayer system.

z axis, respectively [Fig. 11]. The first term is the interaction energy between FM and external magnetic field H, the second term is the FM anisotropic energy, the third term is the AFM anisotropic energy, and the fourth term is the exchange coupling between the FM and AFM interaction energies.

We can assume that $K_{FM}t_{FM} \ll K_{AFM}t_{AFM}$, and then the system energy is

$$E = -HM_{FM}t_{FM}\cos(\theta-\beta) + K_{AFM}t_{AFM}\sin^2\alpha - J_{ex}\cos(\beta-\alpha). \tag{A2}$$

When $\theta = 0$, which is H//easy-axis z, we can get the system energy:

$$E = -HM_{FM}t_{FM}\cos\beta + K_{AFM}t_{AFM}\sin^2\alpha - J_{ex}\cos(\beta-\alpha). \tag{A3}$$

The system energy is minimized by satisfying the conditions:

$$\begin{aligned} \frac{\partial E}{\partial \beta} &= HM_{FM}t_{FM}\sin\beta + J_{ex}\sin(\beta-\alpha) = 0, \\ \frac{\partial E}{\partial \alpha} &= K_{AFM}t_{AFM}\sin 2\alpha - J_{ex}\sin(\beta-\alpha) = 0 \\ AC - B^2 &> 0 \text{ and } A > 0, \end{aligned} \tag{A4}$$

where

$$\begin{aligned} \frac{\partial^2 E}{\partial \alpha^2} &= 2K_{AFM}t_{AFM}\cos 2\alpha + J_{ex}\cos(\beta-\alpha) = A, \\ \frac{\partial^2 E}{\partial \alpha \partial \beta} &= -J_{ex}\cos(\beta-\alpha) = B, \\ \frac{\partial^2 E}{\partial \beta^2} &= HM_{FM}t_{FM}\cos\beta + J_{ex}\cos(\beta-\alpha) = C. \end{aligned} \tag{A5}$$

If $\alpha = \beta = 0$, that is, the magnetic moment is along the easy axis, and $M_{FM} = M_s$; M_s is the saturation magnetization strength of the FM layer. Where

$$AC - B^2 = (2K_{AFM}t_{AFM} + HM_{FM}t_{FM})J_{ex} + 2K_{AFM}t_{AFM}HM_{FM}t_{FM} > 0, \tag{A6}$$

which is

$$H > -\frac{2K_{AFM}t_{AFM}J_{ex}}{2K_{AFM}t_{AFM}M_st_{FM} + J_{ex}M_st_{FM}} = -H_c. \tag{A7}$$

We can get the coercivity of the bilayers:

$$H_c = \frac{2K_{AFM}t_{AFM}J_{ex}}{2K_{AFM}t_{AFM}M_st_{FM} + J_{ex}M_st_{FM}}. \tag{A8}$$

(a) If $K_{AFM}t_{AFM} \gg J_{ex}$, then $H_c \approx J_{ex}/M_st_{FM}$. H_c is only related to the saturation magnetization, M_s, and thickness of FM.

(b) If $K_{AFM}t_{AFM} \ll J_{ex}$, then $H_c \approx 2K_{AFM}t_{AFM}/M_st_{FM}$. H_c is not only related to the thickness of the FM layer, but also to the thickness and anisotropy of AFM. This is consistent with our experimental results.

[1] J. C. Tung and G. Y. Guo, High spin polarization of the anomalous Hall current in Co-based Heusler compounds, New J. Phys. **15**, 033014 (2013).

[2] M. Jourdan, J. Minár, J. Braun, A. Kronenberg, S. Chadov, B. Balke, A. Gloskovskii, M. Kolbe, H. J. Elmers, G. Schönhense, *et al.*, Direct observation of half-metallicity in the Heusler compound Co_2MnSi, Nat. Commun. **5**, 1 (2014).

[3] M. Oogane, T. Kubota, Y. Kota, S. Mizukami, H. Naganuma, A. Sakuma, and Y. Ando, Gilbert magnetic damping constant of epitaxially grown Co-based Heusler alloy thin films, Appl. Phys. Lett. **96**, 252501 (2010).

[4] L. Song, W. Yan, H. L. Wang, J. H. Zhao, and X. H. Zhang, Resonant enhancement of magnetic damping driven by coherent acoustic phonons in thin Co_2FeAl film epitaxied on GaAs, J. Semicond. **42**, 032501 (2021).

[5] W. Wang, E. Liu, M. Kodzuka, H. Sukegawa, M. Wojcik, E. Jedryka, G. H. Wu, K. Inomata, S. Mitani, and K. Hono, Coherent tunneling and giant tunneling magnetoresistance in $Co_2FeAl/MgO/CoFe$ magnetic tunneling junctions, Phys. Rev. B **81**, 140402(R) (2010).

[6] K. Kunimatsu, T. Tsuchiya, T. Roy, K. Elphick, T. Ichinose, M. Tsujikawa, A. Hirohata, M. Shirai, and S. Mizukami, Magnetic tunnel junctions with metastable bcc Co_3Mn electrodes, Appl. Phys. Express **13**, 083007 (2020).

[7] S. Ikeda, K. Miura, H. Yamamoto, K. Mizunuma, H. D. Gan, M. Endo, S. Kanai, J. Hayakawa, F. Matsukura, and H. Ohno, A perpendicular-anisotropy CoFeB–MgO magnetic tunnel junction, Nat. Mater. **9**, 721 (2010).

[8] S. W. Chung, *et al.*, in *2016 IEEE International Electron Devices Meeting (IEDM)* (IEEE, 2016), pp. 27.1.1.

[9] A. C. Sun, F. T. Yuan, J. H. Hsu, and H. Y. Lee, Evolution of structure and magnetic properties of sputter-deposited CoPt thin films on MgO (111) substrates: Formation of the $L1_1$ phase, Scr. Mater. **61**, 713 (2009).

[10] Z. F. Yu, J. Lu, H. L. Wang, X. P. Zhao, D. H. Wei, J. L. Ma, S. W. Mao, and J. H. Zhao, Tunable perpendicular magnetic anisotropy in off-stoichiometric full-Heusler alloy Co_2MnAl, Chin. Phys. Lett. **36**, 067502 (2019).

[11] Z. F. Yu, H. L. Wang, J. L. Ma, S. C. Tong, and J. H. Zhao, Magneto-transport properties of the off-stoichiometric Co_2MnAl film epitaxially grown on GaAs (001), J. Semicond. **40**, 052501 (2019).

[12] S. Bandiera, R. C. Sousa, B. Rodmacq, and B. Dieny, Enhancement of perpendicular magnetic anisotropy through reduction of Co-Pt interdiffusion in (Co/Pt) multilayers, Appl. Phys. Lett. **100**, 142410 (2012).

[13] S. K. Kim and S. C. Shin, Alloy-like Co environment in Co/Pd multilayer films having perpendicular magnetic anisotropy, J. Appl. Phys. **89**, 3055 (2001).

[14] M. S. Gabor, M. Nasui, and A. Timar-Gabor, Perpendicular magnetic anisotropy in Pt/Co-based full Heusler alloy/MgO thin-film structures, Phys. Rev. B **100**, 144438 (2019).

[15] W. H. Meiklejohn and C. P. Bean, New magnetic anisotropy, Phys. Rev. **102**, 1413 (1956).

[16] W. Meiklejohn, Exchange anisotropy—a review, J. Appl. Phys. **33**, 1328 (1962).

[17] Y. J. Tang, B. Roos, T. Mewes, S. O. Demokritov, B. Hillebrands, and Y. J. Wang, Enhanced coercivity of exchange-bias Fe/MnPd bilayers, Appl. Phys. Lett. **75**, 707 (1999).

[18] Q. Li, M. Yang, A. T. N'Diaye, C. Klewe, P. Shafer, N. Gao, T. Y. Wang, E. Arenholz, X. Zhang, C. Hwang, *et al.*, Chirality switching of an antiferromagnetic spiral wall and its effect on magnetic anisotropy, Phys. Rev. Mater. **3**, 114415 (2019).

[19] P. Kuświk, P. L. Gastelois, M. M. Soares, H. C. N. Tolentino, M. De Santis, A. Y. Ramos, A. D. Lamirand, M. Przybylski, and J. Kirschner, Effect of CoO/Ni orthogonal exchange coupling on perpendicular anisotropy of Ni films on Pd (001), Phys. Rev. B **91**, 134413 (2015).

[20] B. Y. Wang, P. H. Lin, M. S. Tsai, C. W. Shih, M. J. Lee, C. W. Huang, N. Y. Jih, P. Y. Cheng, and D. H. Wei, Crucial role of interlayer distance for antiferromagnet-induced perpendicular magnetic anisotropy, Phys. Rev. B **92**, 214435 (2015).

[21] B. Y. Wang, C. H. Hsiao, B. X. Liao, C. Y. Hsu, T. H. Li, Y. L. Hsu, Y. M. Lai, M. S. Tsai, T. H. Chuang, and D. H. Wei, Perpendicular magnetic anisotropy induced by NiMn-based antiferromagnetic films with in-plane spin orientations: Roles of interfacial and volume antiferromagnetic moments, Phys. Rev. B **104**, 024424 (2021).

[22] B. Y. Wang, J. Y. Ning, T. H. Li, C. C. Chung, C. Y. Hsu, M. S. Tsai, T. H. Chuang, and D. H. Wei, Antiferromagnet-induced perpendicular magnetic anisotropy in ferromagnetic Co/Fe films with strong in-plane magnetic anisotropy, Phys. Rev. B **105**, 184415 (2022).

[23] J. Hafner and D. Hobbs, Understanding the complex metallic element Mn. II. Geometric frustration in β-Mn, phase stability, and phase transitions, Phys. Rev. B **68**, 014408 (2003).

[24] J. Pohl, M. J. Christensen, D. Huljic, J. Köhler, E. U. Malang, M. Albrecht, and E. Bucher, Comparison of the x-ray diffraction patterns of epitaxial V/δ-Mn, Cr/δ-Mn, and Fe/δ-Mn superlattices on Ge(001), J. Appl. Phys. **81**, 169 (1997).

[25] E. Kentzinger, U. Rücker, W. Caliebe, G. Goerigk, F. Werges, S. Nerger, J. Voigt, W. Schmidt, B. Alefeld, C. Fermon, and Th. Brückel, Structural and magnetic characterization of Fe/δ-Mn thin films, Physica B **276**, 586 (2000).

[26] M. Bode, S. Heinze, A. Kubetzka, O. Pietzsch, M. Hennefarth, M. Getzlaff, R. Wiesendanger, X. Nie, G. Bihlmayer, and S. Blügel, Structural, electronic, and magnetic properties of a Mn monolayer on W (110), Phys. Rev. B **66**, 014425 (2002).

[27] P. Krüger, O. Elmouhssine, C. Demangeat, and J. C. Parlebas, Magnetic structures of bct manganese in the bulk and at the (001) surface, Phys. Rev. B **54**, 6393 (1996).

[28] S. J. Lee, J. P. Goff, G. J. McIntyre, R. C. C. Ward, S. Langridge, T. Charlton, R. Dalgliesh, and D. Mannix, Perpendicular Antiferromagnetic Ordering of Mn and Exchange Anisotropy in Fe/Mn multilayers, Phys. Rev. Lett. **99**, 037204 (2007).

[29] Y. Takeuchi, R. Okuda, J. Igarashi, B. Jinnai, T. Saino, S. Ikeda, S. Fukami, and H. Ohno, Nanometer-thin $L1_0$-MnAl film with B_2-CoAl underlayer for high-speed and high-density STT-MRAM: Structure and magnetic properties, Appl. Phys. Lett. **120**, 052404 (2022).

[30] D. Mauri, E. Kay, D. Scholl, and J. K. Howard, Novel method for determining the anisotropy constant of MnFe in a NiFe/MnFe sandwich, J. Appl. Phys. **62**, 2929 (1987).

[31] J. Nogués and I. K. Schuller, Exchange bias, J. Magn. Magn. Mater. **192**, 203 (1999).

[32] H. Xi and R. M. White, Antiferromagnetic thickness dependence of exchange biasing, Phys. Rev. B **61**, 80 (2000).

[33] J. Wu, J. S. Park, W. Kim, E. Arenholz, M. Liberati, A. Scholl, Y. Z. Wu, C. Hwang, and Z. Q. Qiu, Direct Measurement of Rotatable and Frozen CoO Spins in Exchange Bias System of CoO/Fe/Ag (001), Phys. Rev. Lett. **104**, 217204 (2010).

[34] X. Xu, L. Yin, D. Wei, C. Tian, G. Dong, X. Jin, and Q. Jia, Co/Pt multilayer based magnetic tunnel junctions using perpendicular magnetic anisotropy, Phys. Rev. B **77**, 052403 (2008).

[35] X. M. Cheng, S. Urazhdin, O. Tchernyshyov, C. L. Chien, V. I. Nikitenko, A. J. Shapiro, and R. D. Shull, Antisymmetric Magnetoresistance in Magnetic Multilayers with Perpendicular Anisotropy, Phys. Rev. Lett. **94**, 017203 (2005).

[36] G. Xiang and N. Samarth, Theoretical analysis of the influence of magnetic domain walls on longitudinal and transverse magnetoresistance in tensile strained (Ga, Mn) As epilayers, Phys. Rev. B **76**, 054440 (2007).

[37] R. C. Bhatt, Y. Y. Cheng, L. X. Ye, N. T. Hai, J. C. Wu, and Th. Wu, Modulation of anisotropic magnetoresistance by anomalous hall signal and its application to real-time domain wall velocity measurement, J. Magn. Magn. Mater. **513**, 167120 (2020).

[38] P. Liu, C. Liu, Z. Wang, M. Huang, G. Hu, J. Xiang, C. Feng, C. Chen, Z. Ma, X. Cui, *et al.*, Planar-symmetry-breaking induced antisymmetric magnetoresistance in van der Waals ferromagnet Fe_3GeTe_2, Nano Res. **15**, 2531 (2022).

[39] Y. Su, Y. Meng, H. Shi, L. Wang, X. Cao, Y. Zhang, R. Li, and H. Zhao, Antisymmetric Magnetoresistance due to Domain-Wall Tilting in Perpendicularly Magnetized Films, Phys. Rev. Appl. **17**, 014013 (2022).